



Published in final edited form as:

*Med Image Anal.* 2018 October ; 49: 46–59. doi:10.1016/j.media.2018.07.006.

## A computational method for longitudinal mapping of orientation-specific expansion of cortical surface in infants

Jing Xia<sup>a,b</sup>, Fan Wang<sup>b</sup>, Yu Meng<sup>b</sup>, Zhengwang Wu<sup>b</sup>, Li Wang<sup>b</sup>, Weili Lin<sup>b</sup>, Caiming Zhang<sup>c,d</sup>, Dinggang Shen<sup>b,e,\*</sup>, and Gang Li<sup>b,\*</sup>

<sup>a</sup>Department of Computer Science and Technology, Shandong University, Jinan 250100, China

<sup>b</sup>Department of Radiology and BRIC, University of North Carolina at Chapel Hill, NC 27599, USA

<sup>c</sup>Digital Media Technology Key Lab of Shandong Province, Jinan 250061, China

<sup>d</sup>Department of Software, Shandong University, Jinan 250100, China

<sup>e</sup>Department of Brain and Cognitive Engineering, Korea University, Seoul 02841, Republic of Korea

### Abstract

The cortical surface of the human brain expands dynamically and regionally heterogeneously during the first postnatal year. As all primary and secondary cortical folds as well as many tertiary cortical folds are well established at term birth, the cortical surface area expansion during this stage is largely driven by the increase of surface area in two orthogonal orientations in the tangent plane: 1) the expansion parallel to the folding orientation (i.e., increasing the lengths of folds) and 2) the expansion perpendicular to the folding orientation (i.e., increasing the depths of folds). This information would help us better understand the mechanisms of cortical development and provide important insights into neurodevelopmental disorders, but still remains largely unknown due to lack of dedicated computational methods. To address this issue, we propose a novel method for longitudinal mapping of orientation-specific expansion of cortical surface area in these two orthogonal orientations during early infancy. First, to derive the two orientation fields perpendicular and parallel to cortical folds, we propose to adaptively and smoothly fuse the gradient field of sulcal depth and also the maximum principal direction field, by leveraging their region-specific reliability. Specifically, we formulate this task as a discrete labeling problem, in which each vertex is assigned to an orientation label, and solve it by graph cuts. Then, based on the computed longitudinal deformation of the cortical surface, we estimate the Jacobian matrix at each vertex by solving a least-squares problem and derive its corresponding stretch tensor. Finally, to obtain the orientation-specific cortical surface expansion, we project the stretch tensor into the two orthogonal orientations separately. We have applied the proposed method to 30 healthy infants, and for the first time we revealed the orientation-specific longitudinal cortical surface expansion maps during the first postnatal year.

\*Corresponding authors. dgshen@med.unc.edu (D. Shen), gang\_li@med.unc.edu (G. Li).

## Keywords

Cortical folding; Longitudinal development; Cortical surface expansion; Infant brain development

---

## 1. Introduction

The cerebral cortex of the human brain is a highly convoluted, sheet-like structure of gray matter, with the cortical folds formed during late gestation (Chi et al., 1977; Dubois et al., 2007; Habas et al., 2011; Kim et al., 2016; Zilles et al., 2013). At term birth, although all primary and secondary cortical folds, as well as many tertiary cortical folds, are well established, both brain volume and cortical surface area are only one-third of those of adults (Dubois et al., 2007; Hill et al., 2010; Li et al., 2014a). During the first postnatal year, the cerebral cortex develops dynamically in both structure and function, driven by the underlying complex microstructural changes (Li et al., 2018). Particularly, the cerebral cortex expands 80% in surface area, with regionally-heterogeneous expansion patterns (Geng et al., 2017; Li et al., 2012a; Lyall et al., 2014). Increasing studies also suggest that the abnormal cortical surface area expansion during infancy is related to many neurodevelopment disorders. For example, infants who later develop autism spectrum disorder usually present a larger surface area expansion from 6 to 12 months than the control infants, especially in the middle occipital gyrus, cuneus, and lingual gyrus (Hazlett et al., 2017). Infants with congenital heart disease show an overall decrease in cortical surface area and cortical folding with regional alterations in the lateral sulci, orbitofrontal region, cingulate region, and central sulcus (Ortinou et al., 2013). Infants at high genetic risk for schizophrenia have significantly smaller cortical surface area in the right pars triangularis, in comparison with the control infants (Li et al., 2016).

Essentially, the cortical surface expansion during infancy can be mainly decomposed into two orthogonal directions in the tangent plane of cortical folds: 1) The expansion *parallel* to the folding orientation (i.e., increasing the lengths of cortical folds), denoted as  $\mathbf{p}_a$ ; 2) The expansion *perpendicular* to the folding orientation (i.e., increasing the depths of cortical folds), denoted as  $\mathbf{p}_e$ , as shown in Fig. 1(b) and (c), respectively. Of note, although the emergence of tertiary cortical folds after birth also leads to the increase of cortical surface area, this value is relatively small, compared to the expansion in the tangent plane. This is because the cortical folding degree (gyrification index) only increases 16%, while the cortical surface area expands 80% in the first postnatal year (Li et al., 2012a, 2014b). Hence, studying longitudinal orientation-specific surface expansion can help us better quantify cortical development and understand the underlying mechanisms of cortical development (that cannot be revealed by the conventional studies of surface expansion), thus eventually better modeling the dynamic early brain development (Meng et al., 2017; Nie et al., 2010, 2011; Rekik et al., 2016b, 2017). On the other hand, as many neurodevelopmental disorders are associated with abnormal cortical surface expansion during infancy (Hazlett et al., 2017; Li et al., 2016; Lyall et al., 2014; Ortinau et al., 2013), studying longitudinal orientation-specific cortical surface expansion will also help better localize and understand the abnormality, thus helping early identification of biomarkers and also early diagnosis of these disorders. However, due to lack of dedicated computational methods, our knowledge on

orientation-specific cortical surface expansion during infancy remains scarce. These facts have spurred us to develop the first computational method to fill the gaps in both the methodology and knowledge.

To map the orientation-specific surface expansion, we have to estimate the two orientation fields that are parallel to cortical folds  $\mathbf{p}_a$  and perpendicular to cortical folds  $\mathbf{p}_e$  in the tangent plane of cortical folds. However, this is a challenging task due to the remarkable complexity, irregularity and inter-subject variability of cortical folds. In the literature, several methods used the maximum principal direction field to approximate  $\mathbf{p}_e$  (Boucher et al., 2009, 2011; Li et al., 2009; Rekić et al., 2016a). However, this strategy is only valid on the highly-bended regions at gyral crests and sulcal bottoms, where the maximum principal direction is perpendicular to the folding orientation, consistent with  $\mathbf{p}_e$ . On the flat regions at sulcal walls, as the maximum principal curvature is very small and easily affected by subtle noises, the corresponding maximum principal field is inherently ambiguous, sensitive to noise and unreliable. Consequently, using only the maximum principal direction field often leads to the inaccurate estimation of  $\mathbf{p}_e$ . To handle this issue, in this paper, we propose to adaptively integrate and fuse the gradient field of sulcal depth and the maximum principal direction field. Our motivation is based on our observation that these two fields usually complement to each other. Specifically, on the flat regions with large gradient magnitude of sulcal depth (e.g., sulcal walls), the gradient field of sulcal depth is reliable and informative, while the maximum principal direction field is ambiguous and noisy. In contrast, on the highly-bended regions (e.g., gyral crests and sulcal bottoms), the maximum principal direction field is accurate and informative, while the gradient field of sulcal depth is noisy due to the small and ambiguous gradients. Hence, to derive a single field  $\mathbf{p}_e$  from these two fields, we design an energy function to formulate this as a discrete labeling problem, i.e., assigning an orientation label for each vertex to indicate the orientation  $\mathbf{p}_e$  on the cortical surface. We effectively minimize this energy function by using the graph cuts method (Boykov et al., 2001) to guarantee to achieve a strong local minimum.

Hence, given a pair of longitudinal cortical surfaces with established vertex-to-vertex cortical correspondences, the proposed method for mapping orientation-specific cortical surface expansion consists of four key steps. First, we compute the gradient field of sulcal depth based on the first-order Taylor expansion and the maximum principal direction field via a finite difference method. Second, to estimate the orientation field perpendicular to cortical folds, we adaptively and smoothly fuse the gradient field of sulcal depth and the maximum principal direction field by leveraging their region-specific reliability using the above proposed energy function minimization method. Next, we estimate the Jacobian matrix of the longitudinal deformation of cortical surfaces for each vertex by solving a least-squares problem, and further derive its stretch tensor by removing the rotation component. Finally, to compute orientation-specific surface expansion maps, we project the stretch tensor separately into the orientation field perpendicular to cortical folds and the orientation field parallel to cortical folds. We have applied our method on the longitudinal cortical surfaces of 30 infants with longitudinal scans at both 0 and 1 year of age. For the first time, we revealed the orientation-specific and region-specific cortical surface expansions during the first postnatal year.

## 2. Materials and methods

### 2.1. Subjects and image acquisition

This study has been approved by the Institutional Review Board of the University of North Carolina (UNC) School of Medicine. Pregnant mothers were recruited during the second trimester of pregnancy from the UNC hospitals. Informed consents were obtained from all the parents. Exclusion criteria include abnormalities on fetal ultrasound and major medical or psychotic illness of the mother. All infants were free of congenital anomalies, metabolic disease, and focal lesions.

Longitudinal brain MRI scans at 0 and 1 year of age were acquired from 30 normal infants (17 males/13 females). Before scanning, infants were fed, swaddled, and fitted with ear protection. Infants were scanned unsedated by using a Siemens head-only 3T scanner (Allegra, Siemens Medical System, Erlangen, Germany) with a circular polarized head coil. T1-weighted images (144 sagittal slices) were obtained by using the three-dimensional magnetization-prepared rapid gradient echo (MPRAGE) sequence: TR = 1900 ms, TE = 4.38 ms, inversion time = 1100 ms, Flip Angle = 7°, and resolution =  $1 \times 1 \times 1 \text{ mm}^3$ . T2-weighted images (64 transverse slices) were acquired with turbo spin-echo sequences: TR = 7380 ms, TE = 119 ms, Flip Angle = 150°, and resolution =  $1.25 \times 1.25 \times 1.95 \text{ mm}^3$ .

### 2.2. Image processing and cortical surface mapping

We processed all MR images using the UNC Infant Pipeline (Li et al., 2015) for cortical surface-based analysis. Specifically, the image processing procedure included the following five major steps. First, we automatically removed non-brain tissues, cerebellum and brain stem (Shi et al., 2012). Second, we corrected intensity inhomogeneity using the N3 method (Sled et al., 1998). Third, we rigidly aligned all images at each age to their age-matched infant brain MRI atlas (Shi et al., 2011). Next, we segmented the brain images into white matter (WM), grey matter (GM), and cerebrospinal fluid (CSF) by using an infant-dedicated longitudinally guided coupled level-sets method (Wang et al., 2015; Wang et al., 2014; Wang et al., 2013). Finally, we automatically masked and filled noncortical structures, and separated the left and right hemispheres.

After the above process, based on the segmentation result of each hemisphere, we corrected topological errors in white matter using a sparse representation method (Hao et al., 2016). Then, we reconstructed inner, central and outer cortical surfaces by using a topology-preserving deformable surface method (Li et al., 2014a, 2012b; Nie et al., 2011). Note that the analysis of the orientation-specific cortical surface expansion is based on the central cortical surface, since it provides a more balanced representation of gyral and sulcal regions (Hill et al., 2010; Li et al., 2012a; Van Essen, 2005). Next, we mapped all cortical surfaces onto a standard spherical space (Fischl et al., 1999). To study longitudinal cortical surface expansion, we need to establish both cross-sectional (inter-subject) and longitudinal (intra-subject) vertex-to-vertex cortical correspondences. For establishing longitudinal correspondences, we aligned each spherical surface at 0 year of age onto its corresponding surface at 1 year of age using Spherical Demons (Yeo et al., 2010). Specifically, Spherical Demons aligns cortical surfaces on the spherical space with the mapped cortical folding

patterns represented by several geometric features, including the mean curvature map of the inflated cortical surface, the average convexity map of the cortical surface, and the mean curvature map of the cortical surface. Of note, the average convexity records the accumulated movement for each vertex during surface inflation, reflecting the relatively large-scale geometry of the cortical folding. Therefore, Spherical Demons uses the average convexity map for rough alignment and the mean curvature map of the cortical surface for final fine alignment. For establishing cross-sectional cortical correspondences, we aligned each spherical surface at 1 year of age onto the UNC 4D Infant Cortical Surface Atlas (<https://www.nitrc.org/projects/infantsurfatlas>) (Li et al., 2015). Based on these deformation fields, we then resampled all the cortical surfaces at 1 year of age as a standard-mesh tessellation with 163,842 vertices, thus establishing vertex-to-vertex correspondences across subjects at 1 year of age. We further warped all the resampled surfaces at 1 year of age to their corresponding surfaces at 0 year of age based on the longitudinal surface registration results, thereby establishing vertex-to-vertex correspondences across all subjects and ages.

The sulcal depth map, which provides a continuous measurement of the cortical folding shape attributes, was computed on each cortical surface (Li et al., 2013; Meng et al., 2014). For each vertex, the sulcal depth is defined as its distance to the nearest corresponding vertex on the cerebral hull surface, which is a surface running along the margins of gyri without dipping into sulci (Li et al., 2013; Van Essen, 2005). The first row in Fig. 2 shows the cortical sulcal depth maps of the left hemisphere of a representative individual at 0 year and 1 year of age. As can be observed, the value of sulcal depth is large at the sulcal bottoms, yet small at the gyral crests.

The maximum principal curvature map, which estimates the local shape of the cortical folding, was also computed on each cortical surface (Li et al., 2009, 2013). For each vertex, it is the principal curvature with the largest absolute value in the two principal curvatures. The second row in Fig. 2 shows the maximum principal curvature maps of an infant's cortical surfaces at 0 year and 1 year of age. As can be observed, the maximum principal curvature is large positive and large negative at gyral crests and sulcal bottoms, respectively, yet it is close to zero on the flat region, such as sulcal walls.

### 2.3. Estimating orientation fields of cortical folds

**2.3.1. Motivation**—To map cortical surface expansion in the two orthogonal orientations  $\mathbf{p}_e$  (the orientation perpendicular to the folding orientation) and  $\mathbf{p}_a$  (the orientation parallel to the folding orientation), we have to first accurately estimate these two orientation fields in the tangent plane of cortical folds, as illustrated in Fig. 3(a). However, this is quite challenging due to the highly complex, convoluted and variable cortical folds. Note that, since  $\mathbf{p}_e$  and  $\mathbf{p}_a$  are orthogonal, we can first estimate  $\mathbf{p}_e$  and then derive  $\mathbf{p}_a$  accordingly.

Several methods have been proposed to use the maximum principal direction (the direction corresponding to the maximum principal curvature) to approximate  $\mathbf{p}_e$  (Boucher et al., 2009, 2011; Li et al., 2009; Rekik et al., 2016a). However, this approximation indeed brings ambiguity in certain regions. Actually, the maximum principal direction field is consistent with  $\mathbf{p}_e$  only on the highly-bended regions at gyral crests and sulcal bottoms, as shown by purple ellipses in the left panel of Fig. 4(e). However, for other regions at sulcal walls, the

maximum principal direction field is inconsistent with  $\mathbf{p}_e$ , due to being dominated by either the noises or turning of the folds. An example of the turning fold is shown by green ellipses in the left panel of Fig. 4(h), where the maximum principal direction field is clearly not perpendicular to the major folding orientation anymore. On the flat regions, the maximum principal curvature is very small and inherently sensitive to noise, and thus the corresponding maximum principal direction is ambiguous and could be dramatically changed by subtle noises. An example is shown in the left panels of Fig. 4(f) and (g) delineated by green ellipses.

To address this issue, we propose to leverage both the maximum principal direction and the gradient field of sulcal depth to estimate  $\mathbf{p}_e$ . This is inspired by the fact that, the gradient of sulcal depth, which represents the change of sulcal depth from vertex to vertex, is reliable and consistent with the orientation field perpendicular to folds  $\mathbf{p}_e$ , especially at sulcal walls with large gradient magnitude of sulcal depth. However, at the sulcal bottoms and gyral crests, the gradient field of sulcal depth is typically noisy and unreliable, as shown by green ellipses in the right panels of Fig. 4(e) and (f). This is due to the small and ambiguous gradients, as shown by black ellipses in the right panels of Fig. 4(a) and (b). Hence, the gradient field of sulcal depth and the maximum principal direction field are complementary to each other for the estimation of  $\mathbf{p}_e$ , as summarized in Table 1. Therefore, we will adaptively fuse these two orientation fields to estimate  $\mathbf{p}_e$ , thus capturing reliable and informative directions from both fields and also ensuring the spatial smoothness of  $\mathbf{p}_e$ .

### 2.3.2. Computing gradient field of sulcal depth and maximum principal direction field

—First, we introduce how to compute the normalized gradient field of sulcal depth (denoted as  $\mathbf{p}_e^g$ ). Letting  $f: M_0 \rightarrow \mathcal{R}$  be the sulcal depth at each vertex on the cortical surface  $M_0$ , the gradient vector of sulcal depth at the vertex  $\mathbf{v}_i$  on the tangent plane is  $\mathbf{g}(\mathbf{v}_i) = \nabla_{M_0} f(\mathbf{v}_i)$ . Note that, unlike in the image space with regular grids, the gradient vector of sulcal depth on the surface manifold cannot be directly computed. Herein, we use the first order of Taylor's theorem to approximate the sulcal depth at vertex  $\mathbf{v}_i$  with its first-ring neighborhood vertex  $\mathbf{v}_j$  on the cortical surface, formulated as:

$$f(\mathbf{v}_i) \approx f(\mathbf{v}_j) + \mathbf{g}(\mathbf{v}_j)^T \cdot (\mathbf{v}_i - \mathbf{v}_j). \quad (1)$$

Hence, to estimate  $\mathbf{g}(\mathbf{v}_i)$ , we minimize the following error that constrains the gradient vector of sulcal depth to sit in the tangent plane:

$$\mathbf{g}(\mathbf{v}_i) = \underset{\hat{\mathbf{g}}}{\operatorname{argmin}} \left\{ \sum_{\mathbf{v}_j \in \mathcal{N}(\mathbf{v}_i)} (f(\mathbf{v}_i) - f(\mathbf{v}_j) - \hat{\mathbf{g}}(\mathbf{v}_i)^T \cdot (\mathbf{v}_i - \mathbf{v}_j))^2 + |\mathcal{N}(\mathbf{v}_i)| (\hat{\mathbf{g}}(\mathbf{v}_i)^T \cdot \mathbf{n}(\mathbf{v}_i))^2 \right\},$$

(2)

where  $\mathcal{N}(\mathbf{v}_i)$  represents the neighborhood of vertex  $\mathbf{v}_i$ ,  $|\mathcal{N}(\mathbf{v}_i)|$  represents the number of neighbors of vertex  $\mathbf{v}_i$ , and  $\mathbf{n}(\mathbf{v}_i)$  is the normal vector of  $\mathbf{v}_i$ . The field  $\mathbf{p}_e^g(\mathbf{v}_i)$  at vertex  $\mathbf{v}_i$  in the tangent plane is obtained by normalizing  $\mathbf{g}(\mathbf{v}_i)$  as:  $\mathbf{p}_e^g(\mathbf{v}_i) = \mathbf{g}(\mathbf{v}_i)/\|\mathbf{g}(\mathbf{v}_i)\|$ , where  $\|\mathbf{g}(\mathbf{v}_i)\|$  is the gradient magnitude of sulcal depth.

Then, we compute the maximum principal curvature  $\mathbf{c}$  and its corresponding maximum principal direction field  $\mathbf{p}_e^c$ , which measure the maximum strength and its corresponding direction of the normal direction variation, respectively, by using the finite difference method (Li et al., 2009). Specifically, we first estimate the Weingarten matrix of the normal direction in each triangle face and then obtain the Weingarten matrix of each vertex by weighted-averaging them in one ring of adjacent faces. The principal curvatures and principal directions at each vertex are the eigenvalues and eigenvectors of the Weingarten matrix, respectively. The maximum principal curvature is the principal curvature with the largest absolute value in the two principal curvatures, and the maximum principal direction is the direction corresponding to the maximum principal curvature (Rusinkiewicz, 2004).

**2.3.3. Deriving the orientation fields of cortical folds**—To estimate  $\mathbf{p}_e$ , we propose to adaptively take regionally-variable advantage of both the normalized gradient field of sulcal depth  $\mathbf{p}_e^g$  and the maximum principal direction field  $\mathbf{p}_e^c$ . As shown in Fig. 4, on the highly-bended regions at gyral crests and sulcal bottoms, the maximum principal direction field  $\mathbf{p}_e^c$  is more reliable and informative for the estimation of  $\mathbf{p}_e$ , as the gradient field of sulcal depth  $\mathbf{p}_e^g$  is typically noisy and unreliable, due to small and ambiguous gradients. On the turning corners and flat regions at sulcal walls, the gradient field  $\mathbf{p}_e^g$  is more reliable and useful for the estimation of  $\mathbf{p}_e$ , due to ambiguity in computing the maximum principal direction field  $\mathbf{p}_e^c$ . On the flat regions at wide sulcal bottoms and gyral crests, both  $\mathbf{p}_e^g$  and  $\mathbf{p}_e^c$  are unreliable and ambiguous, where the reliable and informative direction fields from neighboring regions can be leveraged for the estimation of  $\mathbf{p}_e$ . Hence, we design an energy function to formulate this problem as a discrete labeling problem, i.e., assigning an orientation label  $\mathbf{I}$  indicating the orientation  $\mathbf{p}_e$  for each vertex based on  $\mathbf{p}_e^g$  and  $\mathbf{p}_e^c$  adaptively, and then solve it effectively by using a graph cuts method.

Given the normalized gradient field of sulcal depth  $\mathbf{p}_e^g$  and the maximum principal direction field  $\mathbf{p}_e^c$ , we aim to minimize the following energy function for deriving  $\mathbf{I}(\mathbf{v}_i)$ :

$$E = \sum_{\mathbf{v}_i \in M_0} D(\mathbf{I}(\mathbf{v}_i), \mathbf{p}_e^g(\mathbf{v}_i), \mathbf{p}_e^c(\mathbf{v}_i)) + \sum_{\mathbf{v}_i, \mathbf{v}_j \in \mathcal{N}} S(\mathbf{I}(\mathbf{v}_i), \mathbf{I}(\mathbf{v}_j)). \quad (3)$$

The first term in Eq. (3) is a data term to adaptively keep  $\mathbf{I}(\mathbf{v}_i)$  close to  $\mathbf{p}_e^g(\mathbf{v}_i)$  or  $\mathbf{p}_e^c(\mathbf{v}_i)$ . The second term is a smoothness term to eliminate the unreliable and noisy orientations by

propagating the reliable orientations from neighbors to the problematic regions. For each vertex  $\mathbf{v}_i$ ,  $\mathbf{l}(\mathbf{v}_i)$  is its label from the finite label space, which is defined as 81 orientations uniformly distributed on a unit hemisphere, as shown in Fig. 3(b). Note that, for our application, a direction and its opposite direction will be regarded the same. Herein, the number of orientation labels is determined by gradually increasing the numbers, while visually assessing the resulted orientation field. We found that 81 discrete orientation labels are already dense enough to generate promising results.

The data term, which is jointly determined by  $\mathbf{p}_e^g(\mathbf{v}_i)$  and  $\mathbf{p}_e^c(\mathbf{v}_i)$ , is computed as:

$$D(\mathbf{l}(\mathbf{v}_i), \mathbf{p}_e^g(\mathbf{v}_i), \mathbf{p}_e^c(\mathbf{v}_i)) = W_g(\mathbf{v}_i) \cdot D^g(\mathbf{l}(\mathbf{v}_i), \mathbf{p}_e^g(\mathbf{v}_i)) + W_c(\mathbf{v}_i) \cdot D^c(\mathbf{l}(\mathbf{v}_i), \mathbf{p}_e^c(\mathbf{v}_i)), \quad (4)$$

where  $D^g(\mathbf{l}(\mathbf{v}_i), \mathbf{p}_e^g(\mathbf{v}_i))$  is a gradient-determined term and  $D^c(\mathbf{l}(\mathbf{v}_i), \mathbf{p}_e^c(\mathbf{v}_i))$  is a curvature-determined term. Thus,  $D^g(\mathbf{l}(\mathbf{v}_i), \mathbf{p}_e^g(\mathbf{v}_i))$  and  $D^c(\mathbf{l}(\mathbf{v}_i), \mathbf{p}_e^c(\mathbf{v}_i))$  are, respectively, defined as:

$$D^g(\mathbf{l}(\mathbf{v}_i), \mathbf{p}_e^g(\mathbf{v}_i)) = \min\{\|\mathbf{l}(\mathbf{v}_i) - \mathbf{p}_e^g(\mathbf{v}_i)\|, \|\mathbf{l}(\mathbf{v}_i) - (-\mathbf{p}_e^g(\mathbf{v}_i))\|\}, \quad (5)$$

$$D^c(\mathbf{l}(\mathbf{v}_i), \mathbf{p}_e^c(\mathbf{v}_i)) = \min\{\|\mathbf{l}(\mathbf{v}_i) - \mathbf{p}_e^c(\mathbf{v}_i)\|, \|\mathbf{l}(\mathbf{v}_i) - (-\mathbf{p}_e^c(\mathbf{v}_i))\|\}. \quad (6)$$

Herein,  $w_g(\mathbf{v}_i)$  and  $w_c(\mathbf{v}_i)$  are the two spatially-adaptive weighting parameters, defined as:

$$W_g(\mathbf{v}_i) = 1 - e^{-\lambda_g \|\mathbf{g}(\mathbf{v}_i)\|}, \quad (7)$$

$$W_c(\mathbf{v}_i) = e^{-\lambda_g \|\mathbf{g}(\mathbf{v}_i)\|} \left( 1 - e^{-\lambda_c |c(\mathbf{v}_i)|} \right). \quad (8)$$

where  $\lambda_g$  and  $\lambda_c$  are the non-negative parameters used to determine the trade-off between preserving the gradient field of sulcal depth and preserving the maximum principal direction field. According to Eqs. (7) and (8), on the turning corners and flat regions at sulcal walls, where  $\|\mathbf{g}(\mathbf{v}_i)\|$  is typically large and  $\mathbf{p}_e^g(\mathbf{v}_i)$  is more reliable and informative,  $w_g(\mathbf{v}_i)$  will be large and  $w_c(\mathbf{v}_i)$  will be small, thus encouraging  $\mathbf{l}(\mathbf{v}_i)$  to be close to  $\mathbf{p}_e^g(\mathbf{v}_i)$ . On the highly-bended regions at sulcal bottoms and gyral crests, where  $\|\mathbf{g}(\mathbf{v}_i)\|$  is typically small and  $|c(\mathbf{v}_i)|$  is large,  $\mathbf{p}_e^c(\mathbf{v}_i)$  is more reliable and informative, and thus  $w_g(\mathbf{v}_i)$  will be small and  $w_c(\mathbf{v}_i)$  will be large, encouraging  $\mathbf{l}(\mathbf{v}_i)$  to be close to  $\mathbf{p}_e^c(\mathbf{v}_i)$ .

In the smoothness term of Eq. (3),  $S(\mathbf{l}(\mathbf{v}_i), \mathbf{l}(\mathbf{v}_j))$  is defined as:

$$S(\mathbf{l}(\mathbf{v}_i), \mathbf{l}(\mathbf{v}_j)) = (w_s(\mathbf{v}_i) + w_s(\mathbf{v}_j)) \cdot \min\{\|\mathbf{l}(\mathbf{v}_i) - \mathbf{l}(\mathbf{v}_j)\|, \|\mathbf{l}(\mathbf{v}_i) - (-\mathbf{l}(\mathbf{v}_j))\|\}, \quad (9)$$

$w_s(\mathbf{v}_i)$  is a spatially-adaptive weighting parameter. Ideally,  $w_s(\mathbf{v}_i)$  should be large on regions where both  $\|\mathbf{g}(\mathbf{v}_i)\|$  and  $|c(\mathbf{v}_i)|$  are small, and both  $\mathbf{p}_e^g(\mathbf{v}_i)$  and  $\mathbf{p}_e^c(\mathbf{v}_i)$  are not reliable, e.g., flat regions at wide gyral crests and sulcal bottoms. Hence, this term will enforce the orientation field to be spatially smooth. On the contrary, it should be small on other regions where  $\mathbf{p}_e^g(\mathbf{v}_i)$  and  $\mathbf{p}_e^c(\mathbf{v}_i)$  are very reliable. Therefore,  $w_s(\mathbf{v}_i)$  is defined as:

$$W_S(\mathbf{v}_i) = e^{-\left(\lambda_g \|\mathbf{g}(\mathbf{v}_i)\| + \lambda_c |c(\mathbf{v}_i)|\right)}. \quad (10)$$

The energy function in Eq. (3) is solved by the graph cuts method to obtain the labeled orientations (Boykov et al., 2001). To obtain the final orientation field  $\mathbf{p}_e(\mathbf{v}_i)$  that is perpendicular to the cortical folds,  $\mathbf{l}(\mathbf{v}_i)$  is further projected to the tangent space of the cortical surface and then normalized:

$$\mathbf{p}_e(\mathbf{v}_i) = (\mathbf{l}(\mathbf{v}_i) - (\mathbf{n}(\mathbf{v}_i) \cdot \mathbf{l}(\mathbf{v}_i)) \cdot \mathbf{n}(\mathbf{v}_i)) / \|\mathbf{l}(\mathbf{v}_i) - (\mathbf{n}(\mathbf{v}_i) \cdot \mathbf{l}(\mathbf{v}_i)) \cdot \mathbf{n}(\mathbf{v}_i)\|. \quad (11)$$

Accordingly, the orientation field parallel to folds is computed as:  $\mathbf{p}_a(\mathbf{v}_i) = \mathbf{p}_e(\mathbf{v}_i) \times \mathbf{n}(\mathbf{v}_i)$ .

#### 2.4. Computing Jacobian matrix of longitudinal cortical surface deformation

To map the orientation-specific longitudinal cortical surface expansions, we should also compute the Jacobian matrix of the cortical surface deformation. At each vertex, the Jacobian matrix, which encodes the longitudinal deformation of cortical surfaces, is the spatial gradient of the deformation field. Let  $\mathbf{F}$  be the 3D deformation vector of each vertex on the cortical surface at the first time-point. The Jacobian matrix  $\mathbf{J}$  is then defined by:

$$\mathbf{J} = \begin{pmatrix} \frac{\partial \mathbf{F}_x}{\partial x} & \frac{\partial \mathbf{F}_x}{\partial y} & \frac{\partial \mathbf{F}_x}{\partial z} \\ \frac{\partial \mathbf{F}_y}{\partial x} & \frac{\partial \mathbf{F}_y}{\partial y} & \frac{\partial \mathbf{F}_y}{\partial z} \\ \frac{\partial \mathbf{F}_z}{\partial x} & \frac{\partial \mathbf{F}_z}{\partial y} & \frac{\partial \mathbf{F}_z}{\partial z} \end{pmatrix}. \quad (12)$$

However, unlike in the volumetric image space with regular grids, the Jacobian matrix on the surface manifold cannot be directly computed. To address this issue, we approximated the Jacobian matrix at the vertex  $\mathbf{v}_i$  based on each of its first-ring neighborhood vertex  $\mathbf{v}_j$ , such that:

$$\mathbf{F}(\mathbf{v}_i) \approx \mathbf{F}(\mathbf{v}_j) + \mathbf{J}(\mathbf{v}_i) \cdot (\mathbf{v}_i - \mathbf{v}_j). \quad (13)$$

Therefore, by minimizing the following error, the Jacobian matrix  $\mathbf{J}(\mathbf{v}_i)$  is estimated as:

$$\mathbf{J}(\mathbf{v}_i) = \underset{\hat{\mathbf{J}}}{\operatorname{argmin}} \left\{ \sum_{\mathbf{v}_j \in \mathcal{N}(\mathbf{v}_i)} \left( \mathbf{F}(\mathbf{v}_i) - \mathbf{F}(\mathbf{v}_j) - \hat{\mathbf{J}}(\mathbf{v}_i) \cdot (\mathbf{v}_i - \mathbf{v}_j) \right)^2 \right\}. \quad (14)$$

Note that, the Jacobian matrix encodes both stretch (zooms and shears) and rotational components (Rajagopalan et al., 2012). The first part describes the stretch of the cortical surface, which is desired. The second part contains only the rigid deformation, which is useless in our application. The stretch component is obtained by decomposing the Jacobian matrix according to the polar decomposition theorem (Ogden, 1997):

$$\mathbf{J} = \mathbf{R}\mathbf{S} = \mathbf{S}'\mathbf{R}, \quad (15)$$

where  $\mathbf{R}$  is the rotation matrix and  $\mathbf{S}$  is the stretch tensor, which is a symmetric positive definite matrix. The matrix  $\mathbf{S}$  can be derived as:

$$\mathbf{S} = (\mathbf{J}^T \mathbf{J})^{1/2}. \quad (16)$$

Herein,  $\mathbf{S}$  is a  $3 \times 3$  matrix, which is computed for each vertex  $\mathbf{v}_i$ .

## 2.5. Mapping orientation-specific cortical surface expansion

For each vertex, given the surface deformation matrix  $\mathbf{S}$  and the two orthogonal orientation fields  $\mathbf{p}_e$  and  $\mathbf{p}_a$ , we compute the longitudinal cortical surface expansion in the orientation fields perpendicular to folds as  $s_e$  and parallel to folds as  $s_a$ :

$$S_e = \mathbf{p}_e^T \mathbf{S} \mathbf{p}_e, \quad S_a = \mathbf{p}_a^T \mathbf{S} \mathbf{p}_a. \quad (17)$$

## 3. Results

In this section, we applied the proposed algorithm to longitudinal infant cortical surfaces and for the first time revealed the orientation-specific and region-specific cortical surface expansion during the first postnatal year.

### 3.1. Parameter setting

Our method contains two non-negative parameters:  $\lambda_g$  and  $\lambda_c$ . To determine appropriate parameter values, we tested many different combinations for  $\lambda_g$  and  $\lambda_c$ , and show

representative results in Fig. 5. For example, when setting  $\lambda_g = 10$  and  $\lambda_c = 1$ , the importance of  $\mathbf{p}_e^g$  is too large compared to  $\mathbf{p}_e^c$ , thus leading inaccurate orientation fields at gyral crests and sulcal bottoms (i.e., blue ellipses in Fig. 5(b)), where  $\mathbf{p}_e^c$  is actually more accurate, but cannot be effectively leveraged. In contrast, when setting  $\lambda_g = 1$  and  $\lambda_c = 10$ , the importance of  $\mathbf{p}_e^c$  is too large compared to  $\mathbf{p}_e^g$ , and the result is less influenced by  $\mathbf{p}_e^g$ , thus leading to inaccurate orientation field at sulcal walls (i.e., green ellipses in Fig. 5(c)). Otherwise, if both parameters take small values, e.g.,  $\lambda_g = 1$  and  $\lambda_c = 1$ , the gradient-determined term and the curvature-determined term are both under-weighted, leading to inaccurate orientation fields at sulcal walls (i.e., green ellipses in Fig. 5(d)) and the highly-bended regions at gyral crests and sulcal bottoms (i.e., blue ellipses in Fig. 5(d)). While, if both parameters take too large values, e.g.,  $\lambda_g = 10$  and  $\lambda_c = 10$ , the smooth term and curvature-determined term are under-weighted, leading to inaccurate orientation field on both flat and highly-bended regions at gyral crests and sulcal bottoms (i.e., purple and blue ellipses in Fig. 5(e)). We finally set the parameters as  $\lambda_g = 2$  and  $\lambda_c = 4$  accordingly, as shown in Fig. 5(f).

### 3.2. Evaluation of estimated orientation fields of cortical folds

To evaluate the quality of our estimated orientation field  $\mathbf{p}_e$  of cortical folds, we compared the proposed method with the orientation fields obtained by different methods, i.e., the maximum principal direction field  $\mathbf{p}_e^c$ , the diffused  $\mathbf{p}_e^c$  by the method in (Li et al., 2009), and the gradient field of sulcal depth  $\mathbf{p}_e^g$ . Fig. 6 shows the results of the estimated orientation fields in the regions selected in Fig. 4. As shown in Fig. 6, our proposed method leveraging both  $\mathbf{p}_e^c$  and  $\mathbf{p}_e^g$  can estimate more accurate orientation field perpendicular to the cortical folds at various regions, including sulcal walls, flat and highly-bended regions at gyral crests and sulcal bottoms.

As there is no ground truth for the orientation fields on the cortical surface, to quantitatively evaluate the results, we defined a coherence measurement for an orientation field  $\mathbf{p}$  at each vertex  $\mathbf{v}_i$  as:

$$\text{Coh}(\mathbf{p}(\mathbf{v}_i)) = \frac{1}{|\mathcal{N}(\mathbf{v}_i)|} \sum_{\mathbf{v}_j \in \mathcal{N}(\mathbf{v}_i)} |\mathbf{p}(\mathbf{v}_i) \cdot \mathbf{p}(\mathbf{v}_j)|. \quad (18)$$

The value of Coh ranges from 0 to 1. Larger coherence values indicate that the orientation field is smoother and more coherent. Therefore, this coherence measurement can reflect the performance of the orientation field to some extent. Ideally, we hope the coherence value of  $\mathbf{p}_e$  is similar to the coherence value of  $\mathbf{p}_e^c$  at gyral crests and sulcal bottoms, while similar to that of  $\mathbf{p}_e^g$  at sulcal walls. Fig. 7 shows the coherence values of  $\mathbf{p}_e^c$ , diffused  $\mathbf{p}_e^c$ ,  $\mathbf{p}_e^g$  and  $\mathbf{p}_e$  on a randomly-selected individual cortical surface. Apparently, in the maximum principal direction field  $\mathbf{p}_e^c$ , the large coherence value regions are mostly at gyral crests and sulcal

bottoms, and small coherent regions are mostly at sulcal walls, shown in Fig. 7(a). In the diffused maximum principal direction field  $\mathbf{p}_e^c$  (Li et al., 2009), the coherence is larger at sulcal walls than that of  $\mathbf{p}_e^c$  as shown in Fig. 7(b), but still not promising. In the gradient field of sulcal depth  $\mathbf{p}_e^g$ , the large coherence value regions are mostly at sulcal walls, and small coherence value regions are mostly at gyral crests and sulcal bottoms, as shown in Fig. 7(c). In our estimated orientation field  $\mathbf{p}_e$ , the coherence values are large at gyral crests and sulcal bottoms, as well as at sulcal walls, preserving the regions with large coherence patterns in  $\mathbf{p}_e^c$  and  $\mathbf{p}_e^g$ , as shown in Fig. 7(d). Note that, our estimated orientation field  $\mathbf{p}_e$  also has large coherence values on the flat regions at gyral crests and sulcal bottoms, where the coherence values are low in both  $\mathbf{p}_e^c$  and  $\mathbf{p}_e^g$ .

Fig. 8 shows a comparison of the histogram distributions of coherence measurement in  $\mathbf{p}_e^c$ , the diffused  $\mathbf{p}_e^c$ ,  $\mathbf{p}_e^g$  and  $\mathbf{p}_e$  on the cortical surface in Fig. 7. As can be observed, the shift towards larger values in the histogram of  $\mathbf{p}_e$  indicates that the orientation field is smoother and more coherent in  $\mathbf{p}_e$ , compared to  $\mathbf{p}_e^c$ , diffused  $\mathbf{p}_e^c$ , and  $\mathbf{p}_e^g$ . We also present the histogram distributions at gyral crests and sulcal bottoms as well as sulcal walls, respectively, as shown in Fig. 8(b) and (c). As can be observed, the coherence in  $\mathbf{p}_e$  is larger than that in  $\mathbf{p}_e^c$  at gyral crests and sulcal bottoms, indicating that the orientation field  $\mathbf{p}_e$  is smoother and more coherent than  $\mathbf{p}_e^c$  at those regions. Moreover, the coherence in  $\mathbf{p}_e$  is larger than that in  $\mathbf{p}_e^g$  at sulcal walls, indicating that the orientation field  $\mathbf{p}_e$  is smoother and more coherent than  $\mathbf{p}_e^g$  at those regions. Across 30 infants, the average coherences of the orientation fields on the cortical surfaces in  $\mathbf{p}_e^c$ , diffused  $\mathbf{p}_e^c$ ,  $\mathbf{p}_e^g$  and  $\mathbf{p}_e$  are 0.84, 0.86, 0.88, and 0.94 respectively. Apparently, the coherence in  $\mathbf{p}_e$  is the largest, indicating that our estimated orientation fields have the best smoothness and coherence.

### 3.3. Orientation-specific cortical surface expansion in the first year

By applying our proposed method onto 30 normal infants with longitudinal cortical surfaces at 0 and 1 year of age, for the first time, we explored the orientation-specific surface expansion maps  $s_e$  (in the orientation field perpendicular to cortical folds) and  $s_a$  (in the orientation field parallel to cortical folds). Table 2 provides the mean and standard deviation of the longitudinal cortical surface expansion perpendicular and parallel to the cortical folds of 30 subjects in the first postnatal year. Overall, the cortical surface area expands about 31.47% in the orientation field perpendicular to cortical folds while 31.53% in the orientation field parallel to cortical folds during the first year. By using paired  $t$ -test, the cortical surface expansion perpendicular and parallel to cortical folds of the right hemisphere is statistically larger than that of the left hemisphere ( $p < 0.01$ ). By using unpaired  $t$ -test, the cortical surface expansion in the two orthogonal orientation fields of female is statistically larger than that of male in each hemisphere ( $p < 0.01$ ).

Fig. 9(a) and (b) show the cortical surface expansion maps  $s_e$  and  $s_a$  on the left hemisphere, from 3 randomly-selected individuals. As we can see, the overall spatial patterns of the orientation-specific surface expansion are similar across individuals. To further validate our results, we compare the products of our computed expansion maps in the two orthogonal orientation fields, as shown in Fig. 9(d), with the surface expansion maps computed based on the longitudinal ratio of local cortical surface area, as shown in Fig. 9(e). As we can see, these two maps are very similar, indicating that our results are meaningful. Of note, the subtle differences between the two maps might be related to the emergence of tertiary cortical folds after birth.

### 3.3.1. Surface expansion in orientations *perpendicular* to cortical folds—Fig.

10(a) shows the population-average cortical surface expansion maps  $s_e$  in the orientation field perpendicular to cortical folds in the first postnatal year. The cortical surface expands remarkably in the orientation perpendicular to folds; however, the expansion is highly nonuniform across different cortical regions. In general, the expansions perpendicular to cortical folds in the parietal, temporal, and occipital lobes are larger than those of the frontal lobe. Specifically, high-expansion regions perpendicular to cortical folds are concentrated in the superior parietal cortex, inferior parietal cortex, lateral occipital cortex, anterior middle temporal gyrus, a portion of the precuneus cortex, and cingulate cortex on both hemispheres.

On the left hemisphere, the postcentral gyrus and transverse temporal cortex are also high-expansion regions. On the right hemisphere, the fusiform gyrus and orbitofrontal cortex are also high-expansion regions. Low-expansion regions are concentrated in the paracentral lobule, entorhinal cortex, temporal pole, precentral gyrus, pars orbitalis, superior frontal gyrus, frontal pole and lateral orbital frontal cortex on both hemispheres. On the left hemisphere, the isthmus-cingulate cortex and the lingual gyrus are also the low-expansion regions. On the right hemisphere, the inferior post-central gyrus is also the low-expansion region. By using paired *t*-test with the significant level as  $p < 0.01$  after corrections for multiple comparisons based on random field theory (Worsley et al., 2004), the red clusters represent the regions with the expansion perpendicular to folds being significantly larger than the average expansion, while the blue clusters represent the regions with the expansion perpendicular to folds being significantly smaller than the average expansion. In general, the regions passing significance are similar in the left and right hemispheres.

### 3.3.2. Surface expansion in orientations *parallel* to cortical folds—Fig. 10(b)

shows the population-average cortical surface expansion maps  $s_e$  of 30 infants in the orientation field parallel to cortical folds in the first year. The cortical surface also expands remarkably in the orientation parallel to cortical folds and regionally heterogeneously. Overall, the surface expansion in the orientation parallel to cortical folds in the parietal, temporal, and occipital lobes are larger than those in the frontal lobe. Specifically, the high-expansion regions parallel to cortical folds are concentrated in the superior parietal cortex, inferior parietal cortex, lateral occipital cortex, anterior temporal cortex, postcentral gyrus, fusiform gyrus, medial orbitofrontal cortex, lingual gyrus, and cuneus cortex on both hemispheres. Low-expansion regions are concentrated in the bottom of middle frontal gyrus, transverse temporal cortex, precentral gyrus, temporal pole, cingulate cortex and

parahippocampal gyrus on both hemispheres. On the left hemisphere, the paracentral lobule is also a low-expansion region. On the right hemisphere, the superior temporal sulcus is also a low-expansion region. By using paired  $t$ -test with the significant level as  $p < 0.01$  after corrections for multiple comparisons (Worsley et al., 2004), the red clusters represent the regions are found to expand parallel to cortical folds significantly larger than the average expansion, while the blue clusters represent the regions are found to expand parallel to cortical folds significantly smaller than the average expansion. In general, the regions passing significance are similar in the two hemispheres.

**3.3.3. Difference of surface expansion in two orthogonal orientations**—Fig. 11 shows the difference of cortical surface expansion maps in the orientations perpendicular to folds  $s_e$  and parallel to folds  $s_a$  of the 30 infants during the first year of age. Many regions show different expansion degrees in the two orthogonal orientations. Specifically, the transverse temporal cortex, posterior middle temporal gyrus, and cingulate cortex exhibit larger expansions in the orientation field perpendicular to cortical folds than in the orientation field parallel to cortical folds on both hemispheres. On the left hemisphere, a portion of the inferior parietal cortex also exhibits larger expansion in the orientation field perpendicular to cortical folds than in the orientation field parallel to folds. On the right hemisphere, the pars triangularis and a portion of medial orbitofrontal cortex exhibit larger expansions in the orientation field perpendicular to cortical folds than in the orientation field parallel to cortical folds. The anterior temporal region, orbitofrontal cortex and medial superior frontal cortex exhibit larger expansions in the orientation field parallel to cortical folds than in the orientation field perpendicular to cortical folds. On the left hemisphere, the pars triangularis, fusiform gyrus, lingual gyrus and a portion of the cuneus cortex exhibit larger expansions in the orientation field parallel to cortical folds than in the orientation field perpendicular to cortical folds. By using paired  $t$ -test with the significant level as  $p < 0.05$  after corrections for multiple comparisons (Worsley et al., 2004), the red clusters represent the cortical regions where the expansion perpendicular to cortical folds is significantly larger than the expansion parallel to cortical folds, whereas the blue clusters represent the cortical regions where the expansion parallel to cortical folds is significantly larger than the expansion perpendicular to cortical folds.

## 4. Discussion and conclusion

In this paper, we proposed a novel method for longitudinal mapping of orientation-specific infant cortical surface expansions in the two orthogonal orientation fields that are perpendicular and parallel to cortical folds. The first step is to estimate the two orthogonal orientation fields on the tangent planes. There are some possible solutions to estimate the cortical orientation fields. On one hand, several methods have proposed to leverage the maximum principal direction field (Boucher et al., 2009, 2011; Li et al., 2009; Rekik et al., 2016a), which is perpendicular to cortical folds on the highly-bended regions (e.g., gyral crests and sulcal bottoms). However, the maximum principal direction field is inherently ambiguous and sensitive to noise on other regions, e.g., sulcal walls as well as flat regions at gyral crests and sulcal bottoms, thus leading to unreliable orientation fields. On the other hand, sulcal fundi could also potentially provide the orientations parallel to cortical folds.

However, there are two limitations when using sulcal fundi for our purpose. First, sulcal fundi are typically extracted based on either sulcal depth or curvature in the state-of-the-art methods (Kao et al., 2006; Li et al., 2010; Lyu et al., 2017; Seong et al., 2010; Shi et al., 2010; Trotter et al., 2012). However, no matter which feature (sulcal depth or curvature) is adopted, the unreliable extraction results always exist in some regions. For example, at turning corners of sulcal banks, curvature-based methods typically lead to noisy sulcal fundi, which are not indicative of the orientations parallel to cortical folds; in asymmetric sulcal bottoms, depth-based methods typically lead to biased sulcal fundi; in very wide and flat sulcal bottoms (e.g., the cingulate sulcus), both curvature-based and depth-based methods cannot reliably locate sulcal fundi. Moreover, long sulcal fundi could be broken in some results. Hence, accurate extraction of sulcal fundi is still a challenging and not well solved problem. Second, even if we can extract sulcal fundi and propagate the orientation fields around sulcal fundi to other cortical regions, it is still difficult to accurately estimate the orientation fields around gyral crests based on sulcal fundi, due to the propagation errors caused by large distances between them.

To accurately derive the cortical orientation fields, we proposed to incorporate the gradient field of sulcal depth, whose characteristic was complementary to the maximum principal direction field. Specifically, the gradient field of sulcal depth is perpendicular to cortical folds on sulcal walls, but ambiguous on the highly-bended regions (e.g., gyral crests and sulcal bottoms). To fuse the gradient field of sulcal depth and the maximum principal direction field, we designed an energy function to formulate this as a discrete labeling problem, i.e., assigning an orientation label for each vertex to indicate the fused orientation on the cortical surface. We minimized the energy function effectively by using a graph cut method, which could guarantee to achieve a strong local minimum for our energy function. Then, we estimated the Jacobian matrix of the longitudinal deformation of cortical surfaces for each vertex by solving a least-square problem, and further derived its stretch tensor by removing the rotation component. At last, to compute the surface expansion maps in the orientations perpendicular and parallel to cortical folds, we projected the stretch tensor into these two orthogonal orientations separately.

The proposed method has been applied to 30 normal infants with longitudinal brain MRI scanned at 0 and 1 year of age. For the first time, we have charted the region-specific longitudinal surface expansion maps in the two orthogonal orientations. Overall, in the first year, the product of cortical surface expansions in the two orthogonal orientations is 71.2%, which is generally consistent with the total area expansion rate, computed as the ratio of surface area (Li et al., 2012a; Lyall et al., 2014). Of note, the differences between the two results might be related to the emergence of tertiary cortical folds after birth. Li et al. (2012a) found that the total surface area expansion in parietal, temporal, and occipital lobes is larger than that in the frontal lobe, which is likely related to cellular, functional, and genetic nonuniformities during development. Our results are generally consistent with this finding, but further provide important new insights into the cortical surface expansion in the first year. Specially, the high-expansion regions in both the orientations perpendicular and parallel to cortical folds were found to be concentrated in the middle temporal gyrus, postcentral gyrus (primary somatosensory cortex), superior parietal cortex (involved in multisensory integration (Molholm et al., 2006)), inferior parietal cortex (involved in

receiving auditory, visual, and somatosensory inputs (Rozzi et al., 2008)), as well as lateral occipital cortex (visual cortex) and precuneus cortex. This pattern might reflect the rapid development of the regions associated with visual and sensory functions and their integrations in the first year of age.

Besides the common high-expansion and low-expansion regions in two orientations, the surface expansion perpendicular to cortical folds is larger than the surface expansion parallel to cortical folds in the bilateral transverse temporal cortex (auditory cortex), cingulate cortex, and middle temporal cortex, as well as right inferior and middle frontal gyrus, and left inferior parietal cortex. On the other hand, the surface expansion parallel to cortical folds is larger than the surface expansion perpendicular to cortical folds in the bilateral pars orbitalis, anterior temporal cortex (critical for semantic memory), medial frontal and orbitofrontal cortex (involved in the cognitive processing of decision-making), fusiform gyrus (related with the recognition, including face, body and word recognition (Weiner and Zilles, 2016)), and lingual gyrus (processing vision). This pattern might reflect that the developments of the decision making, recognition and processing vision systems during the first year is more associated with the surface expansion parallel to cortical folds (i.e., increasing the length of cortical folds) than the surface expansion perpendicular to cortical folds. Of note, the basic unit of the neocortex is the cortical minicolumn, a narrow chain of neurons extending vertically across the cortical cellular layers, perpendicular to the pial surface (Mountcastle, 1997), and the neurons are rarely produced after birth in the cerebral cortex (Rakic, 1988). Therefore, the orientation-specific expansion of cortical surface area is likely caused by anisotropic development of cortical minicolumns.

Our study may have clinical implications for understanding abnormal early cortical development in neurodevelopmental disorders associated with abnormal cortical surface expansion during infancy (Hazlett et al., 2017; Li et al., 2016; Lyall et al., 2014; Ortinau et al., 2013). For example, infants who later develop autism spectrum disorder usually present a hyper-expansion of cortical surface area from 6 to 12 months than the control infants (Hazlett et al., 2017). But it is unclear whether the hyper-expansion is mainly contributed by either the expansion parallel to the orientation field of cortical folds or the expansion perpendicular to the orientation field of cortical folds, or both. Our method will enable differentiating the orientation-specific surface expansion in the infants with autism spectrum disorder, and thus help better localize and understand the abnormality for early identification of biomarkers and early diagnosis.

One limitation is that the proposed approach relatively relies on the surface registration quality, which would potentially impact the decomposition of the deformation fields along the parallel and perpendicular directions. In this study, to guarantee a good registration quality, we performed the cortical surface registration using Spherical Demons, which is a state-of-the-art method that uses the average convexity for rough alignment and the mean curvature for final fine alignment, as in FreeSurfer. These cortical folding features are typically informative at sulcal bottoms and gyral crests for longitudinal alignment, thus the registration results around these regions are relatively reliable for estimating longitudinal deformation. In contrast, these features are less informative at regions far away from sulcal bottoms and gyral crests, e.g., the flat regions on sulcal walls, thus the registration around

these regions might be less reliable, thus potentially impacting the decomposition of the longitudinal deformation.

In summary, this paper has three main contributions. First, we developed the first computational pipeline for mapping longitudinal orientation-specific surface expansion in infants. Second, to accurately estimate the orientation fields of cortical folds, we proposed a novel method to adaptively and smoothly fuse the gradient field of sulcal depth and the maximum principal direction field, by minimizing an energy function using graph cuts. Finally, for the first time, we revealed the orientation-specific and region-specific longitudinal cortical surface expansion maps during the first postnatal year. Given the dynamic expansion of cortical surface during the first postnatal year, in the future, we will further apply our methods to study the orientation-specific cortical surface expansions at temporally dense time points, e.g., every three months during the first year. Moreover, we will investigate the underlying neurobiological mechanisms of the orientation-specific surface expansion and their relations to the structural and functional connectivity development. We will also leverage our method to study abnormal cortical expansion in neurodevelopment disorders, such as autism spectrum disorder and schizophrenia.

## Acknowledgements

This work was partially supported by NIH grants (MH100217, MH108914, MH107815, MH109773, MH110274, MH116225, MH113255), National Natural Science Foundation of China (61373078, 61572292, 61332015, 61602277), National Natural Science Foundation of China Joint Fund with Zhejiang Integration of Informatization and Industrialization under Key Project (U1609218), and Nature Science Foundation of Shandong Province of China (ZR2016FQ12).

## References

- Boucher M, Evans A, Siddiqi K, 2009 Oriented morphometry of folds on surfaces. In: International Conference on Information Processing in Medical Imaging Springer, pp. 614–625.
- Boucher M, Evans A, Siddiqi K, 2011 Anisotropic diffusion of tensor fields for fold shape analysis on surfaces In: Information Processing in Medical Imaging. Springer, pp. 271–282,
- Boykov Y, Veksler O, Zabih R, 2001 Fast approximate energy minimization via graph cuts. *IEEE Trans. Pattern Anal. Mach. Intell* 23, 1222–1239.
- Chi JG, Dooling EC, Gilles FH, 1977 Gyral development of the human brain. *Ann. Neurol* 1, 86–93. [PubMed: 560818]
- Dubois J, Benders M, Cachia A, Lazeyras F, Ha-Vinh Leuchter R, Sizonenko S, Borradori-Tolsa C, Mangin J, Hüppi PS, 2007 Mapping the early cortical folding process in the preterm newborn brain. *Cerebral Cortex* 18, 1444–1454. [PubMed: 17934189]
- Fischl B, Sereno MI, Dale AM, 1999 Cortical surface-based analysis: II: inflation, flattening, and a surface-based coordinate system. *Neuroimage* 9, 195–207. [PubMed: 9931269]
- Geng X, Li G, Lu Z, Gao W, Wang L, Shen D, Zhu H, Gilmore JH, 2017 Structural and maturational covariance in early childhood brain development. *Cerebral Cortex* 27, 1795–1807. [PubMed: 26874184]
- Habas PA, Scott JA, Roosta A, Rajagopalan V, Kim K, Rousseau F, Barkovich AJ, Glenn OA, Studholme C, 2011 Early folding patterns and asymmetries of the normal human brain detected from in utero MRI. *Cerebral Cortex* 22, 13–25. [PubMed: 21571694]
- Hao S, Li G, Wang L, Meng Y, Shen D, 2016 Learning-based topological correction for infant cortical surfaces In: International Conference on Medical Image Computing and Computer-Assisted Intervention. Springer, pp. 219–227.

- Hazlett HC, Gu H, Munsell BC, Kim SH, Styner M, Wolff JJ, Elison JT, Swanson MR, Zhu H, Botteron KN, 2017 Early brain development in infants at high risk for autism spectrum disorder. *Nature* 542, 348–351. [PubMed: 28202961]
- Hill J, Dierker D, Neil J, Inder T, Knutsen A, Harwell J, Coalson T, Van Essen D, 2010 A surface-based analysis of hemispheric asymmetries and folding of cerebral cortex in term-born human infants. *J. Neurosci* 30, 2268–2276. [PubMed: 20147553]
- Kao CK, Hofer M, Sapiro G, Stern J, 2006 A geometric method for automatic extraction of sulcal fundi. *IEEE Int. Symp. Biomed. Imaging* 1168–1171.
- Kim H, Lepage C, Maheshwary R, Jeon S, Evans AC, Hess CP, Barkovich AJ, Xu D, 2016 NEOCIVET: Towards accurate morphometry of neonatal gyrfication and clinical applications in preterm newborns. *Neuroimage* 138, 28–42. [PubMed: 27184202]
- Li G, Guo L, Nie J, Liu T, 2009 Automatic cortical sulcal parcellation based on surface principal direction flow field tracking. *Neuroimage* 46, 923–937. [PubMed: 19328234]
- Li G, Guo L, Nie J, Liu T, 2010 An automated pipeline for cortical sulcal fundi extraction. *Med. Image Anal* 14, 343–359. [PubMed: 20219410]
- Li G, Nie J, Wang L, Shi F, Gilmore JH, Lin W, Shen D, 2014a Measuring the dynamic longitudinal cortex development in infants by reconstruction of temporally consistent cortical surfaces. *Neuroimage* 90, 266–279. [PubMed: 24374075]
- Li G, Nie J, Wang L, Shi F, Lin W, Gilmore JH, Shen D, 2012a Mapping region-specific longitudinal cortical surface expansion from birth to 2 years of age. *Cerebral Cortex* 23, 2724–2733. [PubMed: 22923087]
- Li G, Nie J, Wang L, Shi F, Lyall AE, Lin W, Gilmore JH, Shen D, 2013 Mapping longitudinal hemispheric structural asymmetries of the human cerebral cortex from birth to 2 years of age. *Cerebral Cortex* 24, 1289–1300. [PubMed: 23307634]
- Li G, Nie J, Wu G, Wang Y, Shen D, Initiative A.s.D.N., 2012b Consistent reconstruction of cortical surfaces from longitudinal brain MR images. *Neuroimage* 59, 3805–3820. [PubMed: 22119005]
- Li G, Wang L, Shi F, Gilmore JH, Lin W, Shen D, 2015 Construction of 4D high-definition cortical surface atlases of infants: methods and applications. *Med. Image Anal* 25, 22–36. [PubMed: 25980388]
- Li G, Wang L, Shi F, Lyall AE, Ahn M, Peng Z, Zhu H, Lin W, Gilmore JH, Shen D, 2016 Cortical thickness and surface area in neonates at high risk for schizophrenia. *Brain Struct. Funct* 221, 447. [PubMed: 25362539]
- Li G, Wang L, Shi F, Lyall AE, Lin W, Gilmore JH, Shen D, 2014b Mapping longitudinal development of local cortical gyrfication in infants from birth to 2 years of age. *J. Neurosci* 34, 4228–4238. [PubMed: 24647943]
- Li G, Wang L, Yap P-T, Wang F, Wu Z, Meng Y, Dong P, Kim J, Shi F, Reikik I, 2018 Computational neuroanatomy of baby brains: a review. *Neuroimage*..
- Lyall AE, Shi F, Geng X, Woolson S, Li G, Wang L, Hamer RM, Shen D, Gilmore JH, 2014 Dynamic development of regional cortical thickness and surface area in early childhood. *Cerebral Cortex* 25, 2204–2212. [PubMed: 24591525]
- Lyu I, Sun HK, Woodward ND, Styner MA, Landman BA, 2017 TRACE: a topological graph representation for automatic sulcal curve extraction. *IEEE Trans. Medical Imaging* pp, 1–1.
- Meng Y, Li G, Lin W, Gilmore JH, Shen D, 2014 Spatial distribution and longitudinal development of deep cortical sulcal landmarks in infants. *Neuroimage* 100, 206–218. [PubMed: 24945660]
- Meng Y, Li G, Reikik I, Zhang H, Gao Y, Lin W, Shen D, 2017 Can we predict subject-specific dynamic cortical thickness maps during infancy from birth? *Human Brain Mapping* 38, 2865–2874. [PubMed: 28295833]
- Molholm S, Sehatpour P, Mehta AD, Shpaner M, Gomez-Ramirez M, Ortigue S, Dyke JP, Schwartz TH, Foxe JJ, 2006 Audio-visual multisensory integration in superior parietal lobule revealed by human intracranial recordings. *J. Neurophysiol* 96, 721–729. [PubMed: 16687619]
- Mountcastle VB, 1997 The columnar organization of the neocortex. *Brain* 120, 701–722. [PubMed: 9153131]
- Nie J, Guo L, Li G, Faraco C, Miller LS, Liu T, 2010 A computational model of cerebral cortex folding. *J. Theor. Biol* 264, 467–478. [PubMed: 20167224]

- Nie J, Li G, Wang L, Gilmore JH, Lin W, Shen D, 2011 A computational growth model for measuring dynamic cortical development in the first year of life. *Cerebral Cortex* 22, 2272–2284. [PubMed: 22047969]
- Ogden RW, 1997 Non-linear elastic deformations. Courier Corp..
- Ortinou C, Alexopoulos D, Dierker D, Van Essen D, Beca J, Inder T, 2013 Cortical folding is altered before surgery in infants with congenital heart disease. *J. Pediatrics* 163, 1507–1510.
- Rajagopalan V, Scott J, Habas PA, Kim K, Rousseau F, Glenn OA, Barkovich AJ, Studholme C, 2012 Mapping directionality specific volume changes using tensor based morphometry: an application to the study of gyrogenesis and lateralization of the human fetal brain. *Neuroimage* 63, 947–958. [PubMed: 22503938]
- Rakic P, 1988 Specification of cerebral cortical areas. *Science* 241, 170. [PubMed: 3291116]
- Rekik I, Li G, Lin W, Shen D, 2016a Multidirectional and topography-based dynamic-scale varifold representations with application to matching developing cortical surfaces. *Neuroimage* 135, 152–162. [PubMed: 27138207]
- Rekik I, Li G, Lin W, Shen D, 2016b Predicting infant cortical surface development using a 4D varifold-based learning framework and local topography-based shape morphing. *Med. Image Anal* 28, 1–12. [PubMed: 26619188]
- Rekik I, Li G, Yap P-T, Chen G, Lin W, Shen D, 2017 Joint prediction of longitudinal development of cortical surfaces and white matter fibers from neonatal MRI. *Neuroimage* 152, 411–424. [PubMed: 28284800]
- Rozzi S, Ferrari PF, Bonini L, Rizzolatti G, Fogassi L, 2008 Functional organization of inferior parietal lobule convexity in the macaque monkey: electrophysiological characterization of motor, sensory and mirror responses and their correlation with cytoarchitectonic areas. *Eur. J. Neurosci* 28, 1569–1588. [PubMed: 18691325]
- Rusinkiewicz S, 2004 Estimating curvatures and their derivatives on triangle meshes. In: *3D Data Processing, Visualization and Transmission, 2004. 3DPVT 2004. Proceedings. 2nd International Symposium on*. IEEE, pp. 486–493.
- Seong JK, Im K, Sang WY, Sang WS, Na DL, Lee JM, 2010 Automatic extraction of sulcal lines on cortical surfaces based on anisotropic geodesic distance. *Neuroimage* 49, 293–302. [PubMed: 19683580]
- Shi F, Wang L, Dai Y, Gilmore JH, Lin W, Shen D, 2012 LABEL: pediatric brain extraction using learning-based meta-algorithm. *Neuroimage* 62, 1975–1986. [PubMed: 22634859]
- Shi F, Yap P-T, Wu G, Jia H, Gilmore JH, Lin W, Shen, atlases from neonates to 1-and 2-year-olds. *PloS One* 6, e18746.
- Shi Y, Sun B, Lai R, Dinov I, Toga AW, 2010 Automated sulci identification via intrinsic modeling of cortical anatomy. *Med. Image Comput. Comput. Assist. Interv* 13, 49–56. [PubMed: 20879382]
- Sled JG, Zijdenbos AP, Evans AC, 1998 A nonparametric method for automatic correction of intensity nonuniformity in MRI data. *IEEE Trans. Med. Imaging* 17, 87–97. [PubMed: 9617910]
- Troter AL, Auzias G, Coulon O, 2012 Automatic sulcal line extraction on cortical surfaces using geodesic path density maps. *Neuroimage* 61, 941–949. [PubMed: 22521478]
- Van Essen DC, 2005 A population-average, landmark-and surface-based (PALS) atlas of human cerebral cortex. *Neuroimage* 28, 635–662. [PubMed: 16172003]
- Wang L, Gao Y, Shi F, Li G, Gilmore JH, Lin W, Shen D, 2015 LINKS: Learning-based multi-source IntegrationN frameworK for Segmentation of infant brain images. *Neuroimage* 108, 160–172. [PubMed: 25541188]
- Wang L, Shi F, Li G, Gao Y, Lin W, Gilmore JH, Shen D, 2014 Segmentation of neonatal brain MR images using patch-driven level sets. *Neuroimage* 84, 141–158. [PubMed: 23968736]
- Wang L, Shi F, Yap PT, Lin W, Gilmore JH, Shen D, 2013 Longitudinally guided level sets for consistent tissue segmentation of neonates. *Human Brain Mapping* 34, 956–972. [PubMed: 22140029]
- Weiner KS, Zilles K, 2016 The anatomical and functional specialization of the fusiform gyrus. *Neuropsychologia* 83, 48–62. [PubMed: 26119921]
- Worsley KJ, Taylor JE, Tomaiuolo F, Lerch J, 2004 Unified univariate and multivariate random field theory. *Neuroimage* 23, S189–S195. [PubMed: 15501088]

- Yeo BT, Sabuncu MR, Vercauteren T, Ayache N, Fischl B, Golland P, 2010 Spherical demons: fast diffeomorphic landmark-free surface registration. *IEEE Trans. Med. Imaging* 29, 650–668. [PubMed: 19709963]
- Zilles K, Palomero-Gallagher N, Amunts K, 2013 Development of cortical folding during evolution and ontogeny. *Trends Neurosci.* 36, 275–284. [PubMed: 23415112]

Author Manuscript

Author Manuscript

Author Manuscript

Author Manuscript

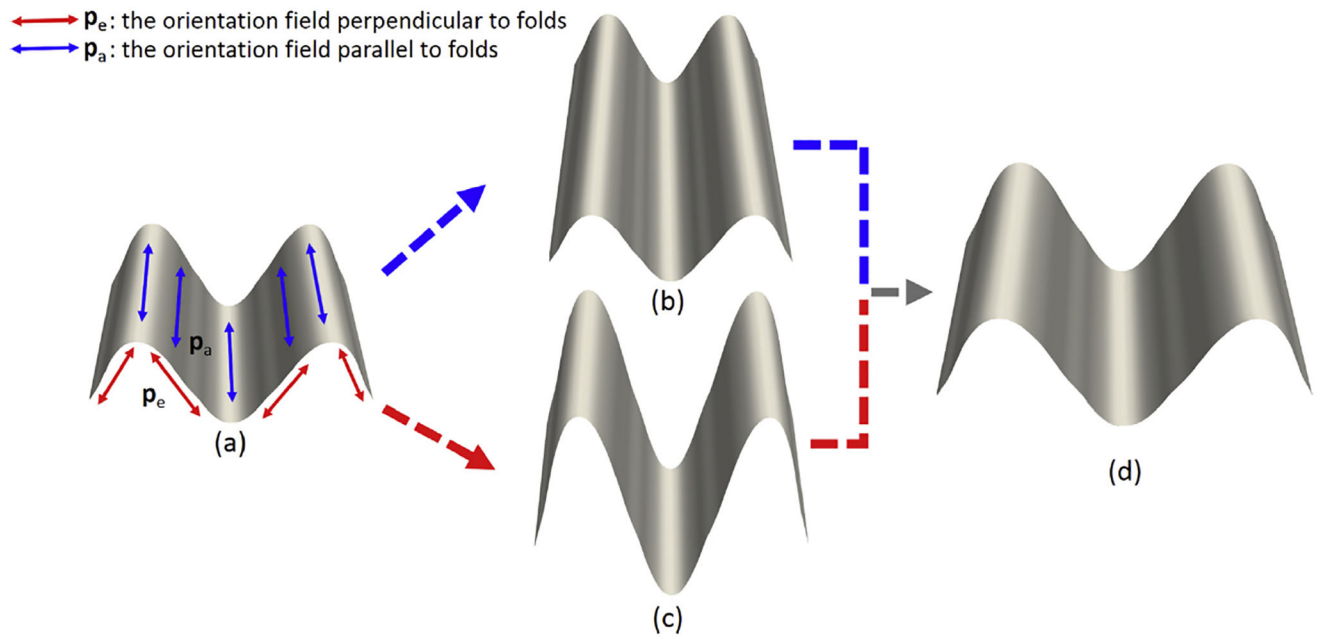


**Fig. 1.**

A schematic illustration of the orientation-specific cortical surface expansion on the tangent planes of synthetic cortical folds. (a) The original folds. (b) Surface expansion in the orientation field parallel to folds  $\mathbf{p}_a$  (i.e., increasing the length of folds). (c) Surface expansion in the orientation field perpendicular to folds  $\mathbf{p}_e$  (i.e., increasing the depth of folds). (d) Surface expansions in both orientations fields  $\mathbf{p}_a$  and  $\mathbf{p}_e$ .

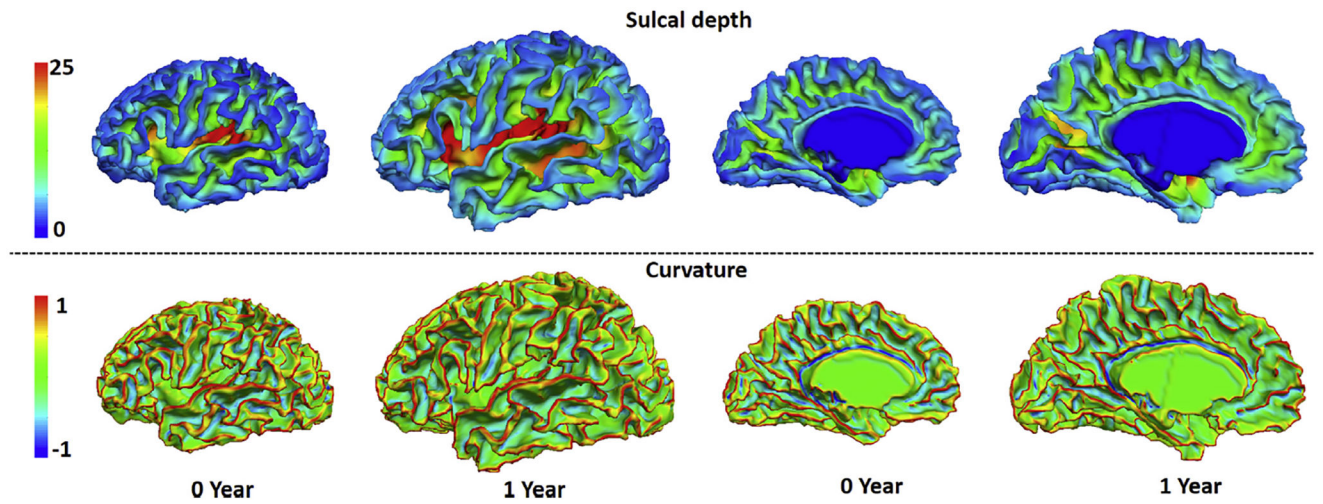


**Fig. 2.** Longitudinal cortical surfaces of the left hemisphere of a representative infant at 0 and 1 year of age. The first row is color-coded by sulcal depth (mm), and the second row is color-coded by the maximum principal curvature.

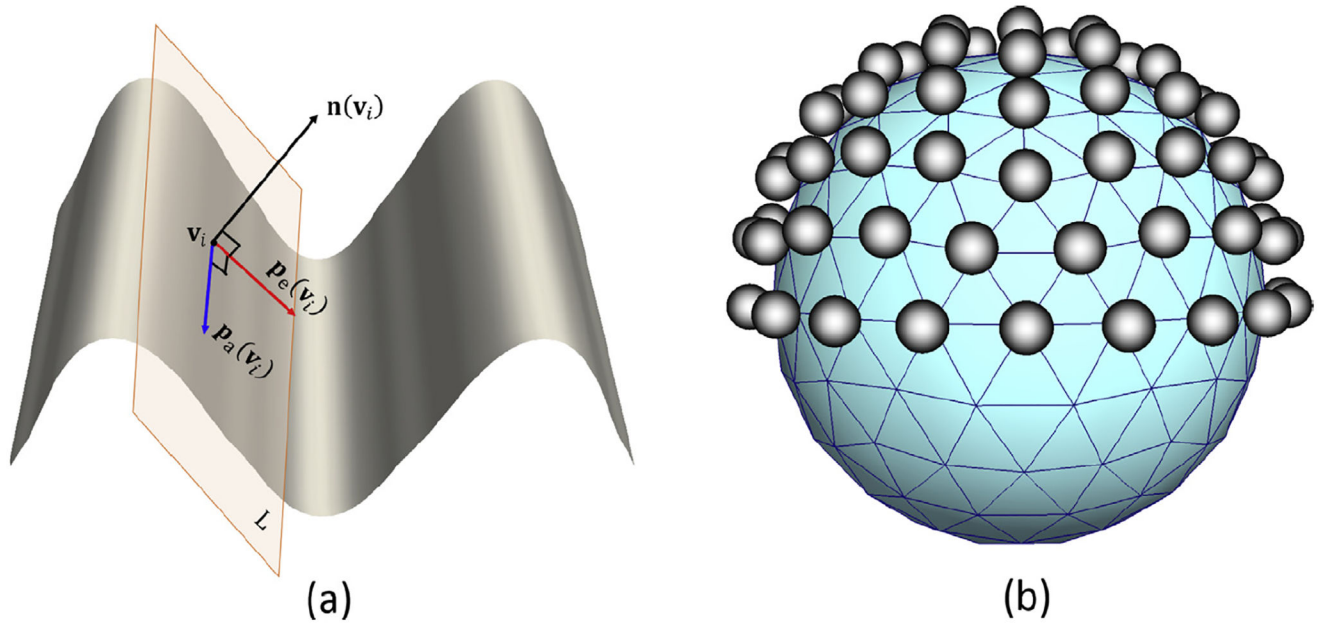


**Fig. 3.** (a) The tangent plane and two orthogonal orientations. (b) The finite label space, where each of the 81 balls represents an orientation.

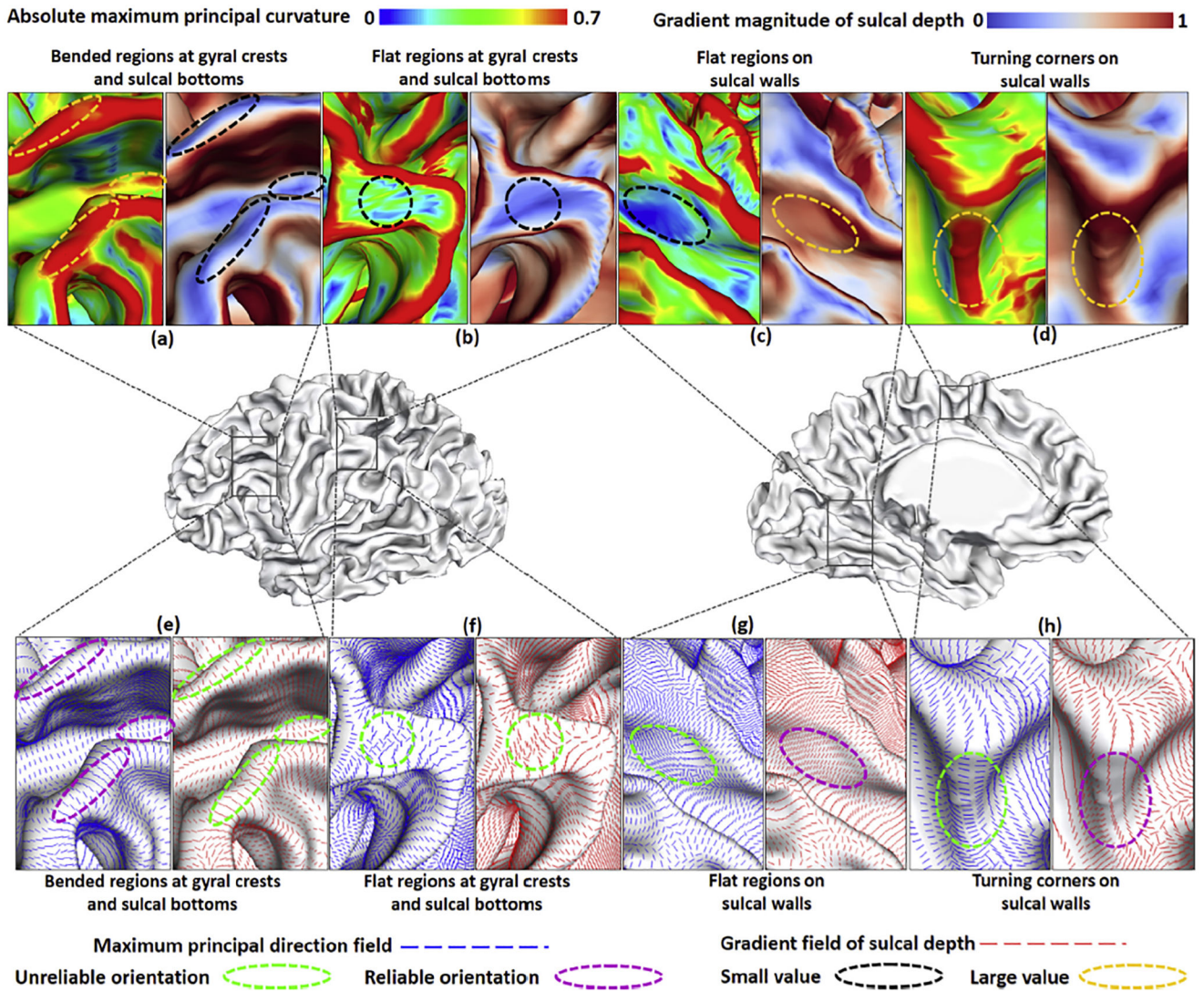


**Fig. 4.** The gradient field of sulcal depth and the maximum principal direction field on the cortical surface of a subject at birth. The left panels in (a)-(d) are color-coded by the absolute maximum principal curvature, and the right panels are color-coded by the gradient magnitude of sulcal depth. The color bars are shown on the top. The left panels in (e)-(h) are the maximum principal direction fields, and the right panels are the gradient fields of sulcal depth. (e)-(h) are the orientation fields at regions corresponding to (a)-(d), respectively. (a) and (e): Bended regions at gyral crests and sulcal bottoms. (b) and (f): Flat regions at gyral crests and sulcal bottoms. (c) and (g): Flat regions at sulcal walls. (d) and (h): The turning corners at sulcal walls. The black and yellow ellipses mark the regions with small and large values, respectively. The purple and green ellipses mark the regions with unreliable and reliable orientations, respectively.

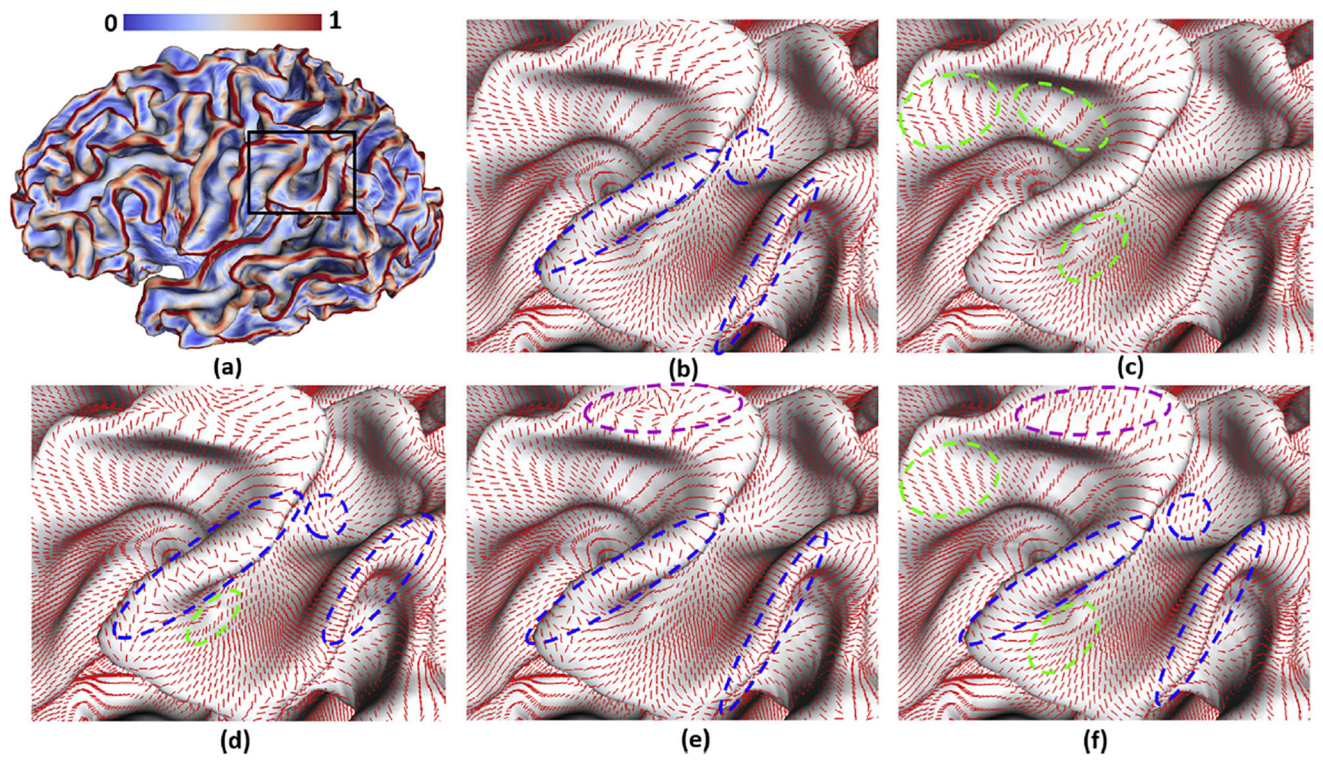


**Fig. 5.** Examples of the estimated orientation field perpendicular to the cortical folds based on different parameters configurations. (a) Gradient magnitude of sulcal depth. (b)  $\lambda_g = 10$  and  $\lambda_c = 1$ . (c)  $\lambda_g = 1$  and  $\lambda_c = 10$ . (d)  $\lambda_g = 1$  and  $\lambda_c = 1$ . (e)  $\lambda_g = 10$  and  $\lambda_c = 10$ . (f)  $\lambda_g = 2$  and  $\lambda_c = 4$ .

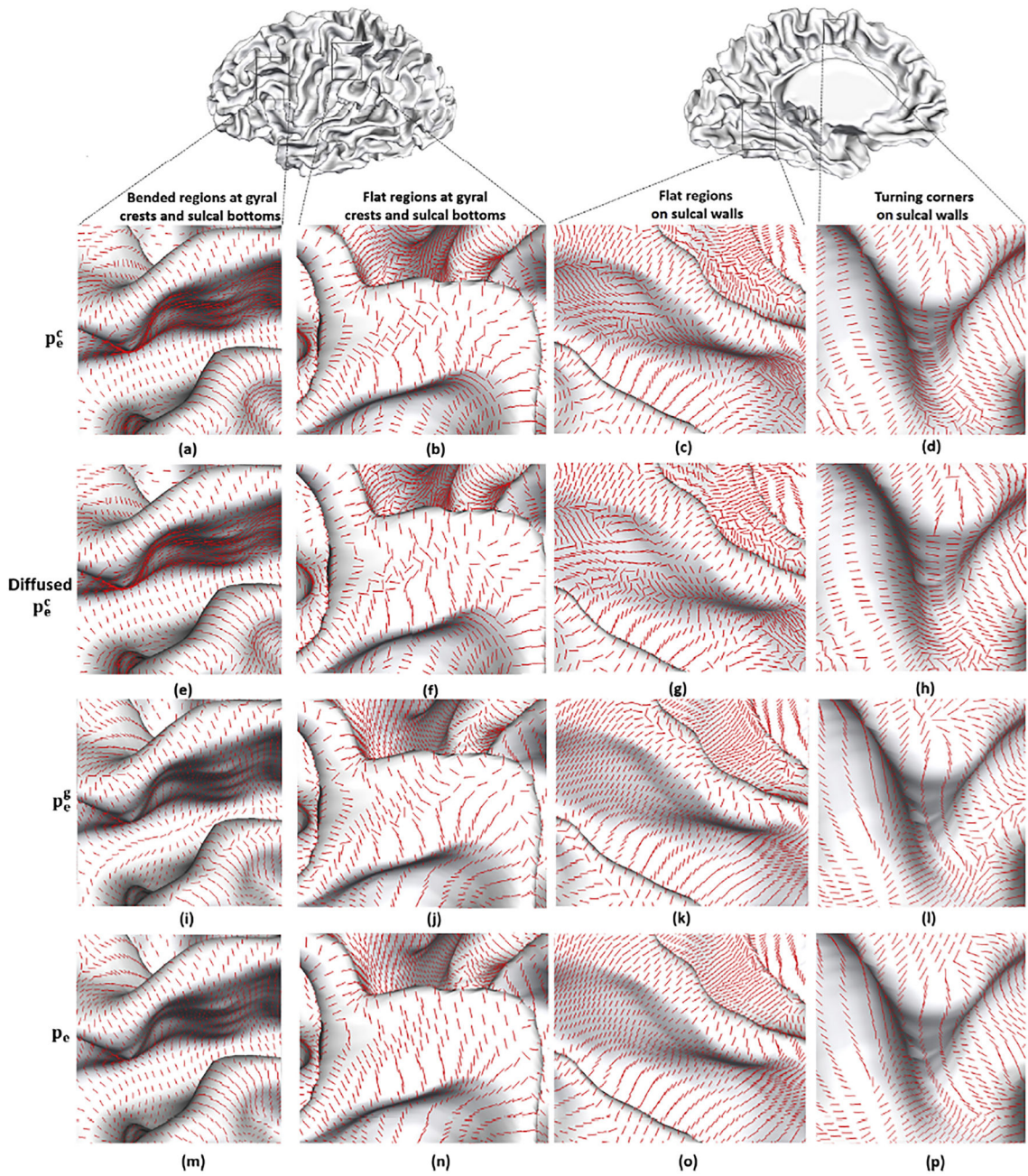


**Fig. 6.** Comparison of the estimated orientation fields at representative regions on an infant cortical surface at 0 year of age by different methods.  $\mathbf{p}_e^c$ : the maximum principal direction field; Diffused  $\mathbf{p}_e^c$ : the diffused maximum principal direction field by the method in Li et al. (2009);  $\mathbf{p}_e^g$ : the gradient field of sulcal depth;  $\mathbf{p}_e$ : the orientation field by the proposed method.

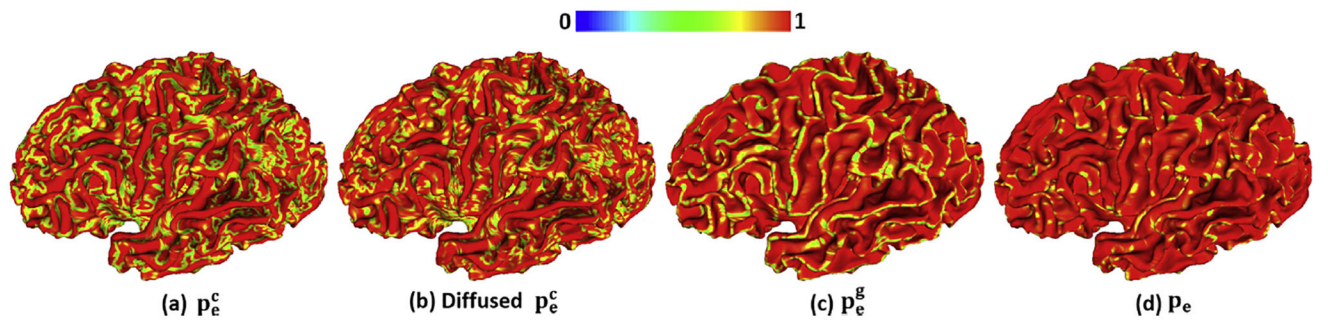


**Fig. 7.**

The coherence maps of the maximum principal direction held  $p_e^c$ , the diffused  $p_e^c$ , the gradient held of sulcal depth  $p_e^g$ , and our estimated orientation field  $p_e$  on a cortical surface.

The color bar is shown on the top.

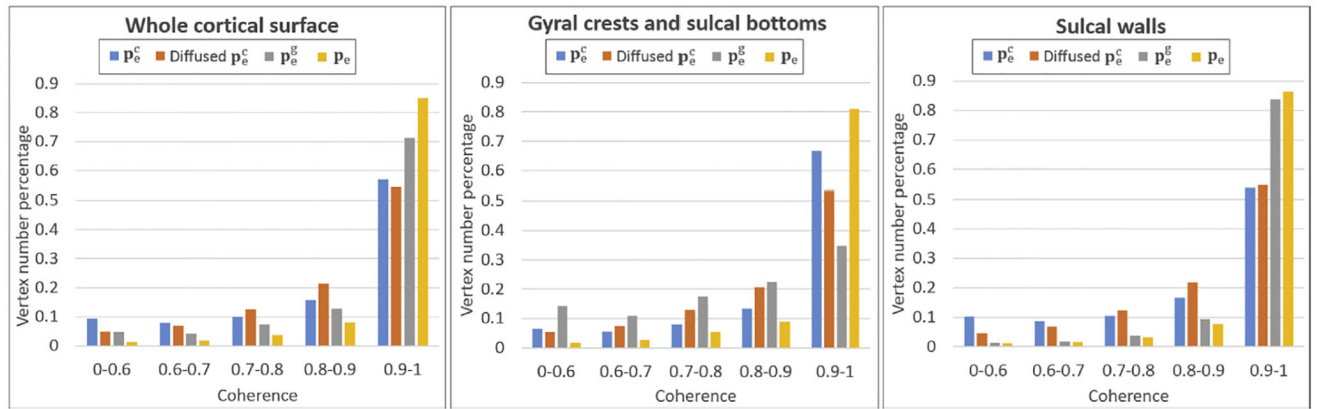


**Fig. 8.**

Comparisons of coherence distributions in  $p_e^c$ , diffused  $p_e^c$ ,  $p_e^g$  and  $p_e$  on a cortical surface. (a)

The comparison on the whole cortical surface. (b) The comparison at gyral crests and sulcal

bottoms. (c) The comparison at sulcal walls.

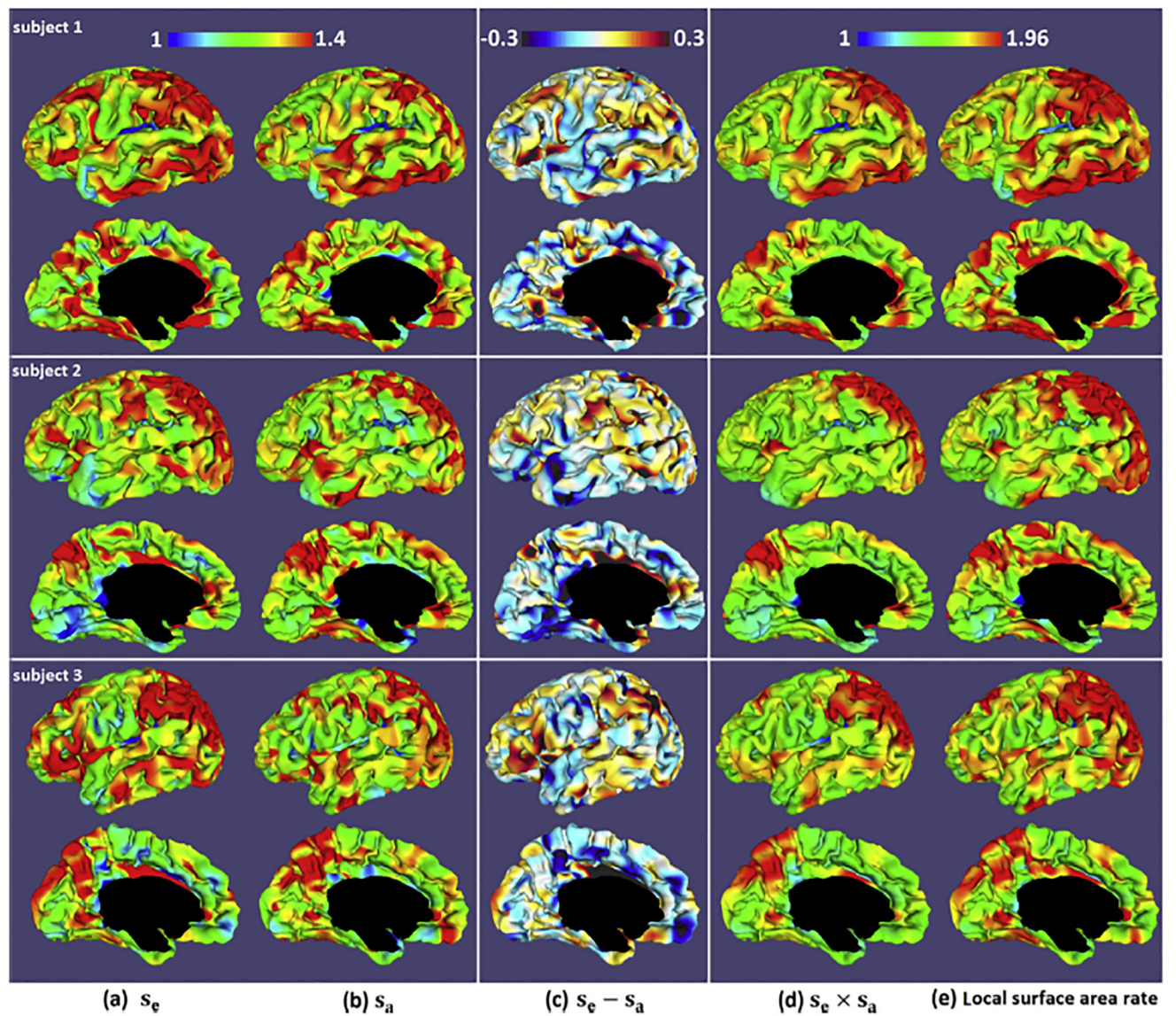


**Fig. 9.**

The orientation-specific cortical surface expansion maps of 3 randomly-selected individuals.

- (a) The expansion maps  $s_e$  in the orientations perpendicular to folds. (b) The expansion maps  $s_a$  in the orientations parallel to folds. (c) The difference of the expansions in the orthogonal orientations in (a) and (b). (d) The product of the expansions in the orthogonal orientations. (e) The expansion maps computed based on the longitudinal ratio of local surface area.

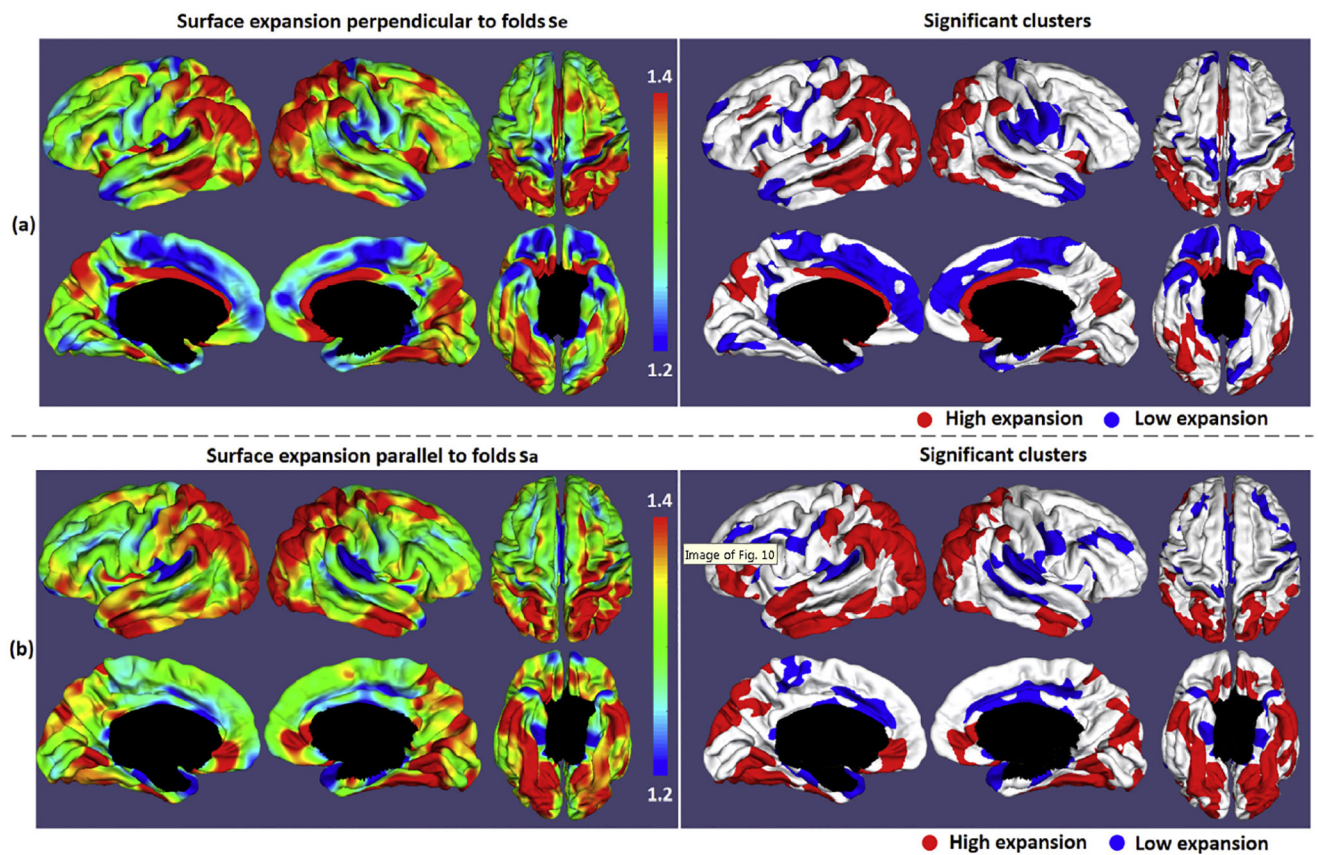


**Fig. 10.**

Longitudinal orientation-specific cortical surface expansions of 30 subjects in the first year. The left column shows the cortical surface expansion maps perpendicular and parallel to cortical folds. The right column shows the significant high-expansion and low-expansion regions ( $p < 0.01$ , after multiple comparisons correction). Red and blue clusters are the high-expansion and low-expansion regions, respectively. (a) Surface expansion perpendicular to cortical folds. (b) Surface expansion parallel to cortical folds.

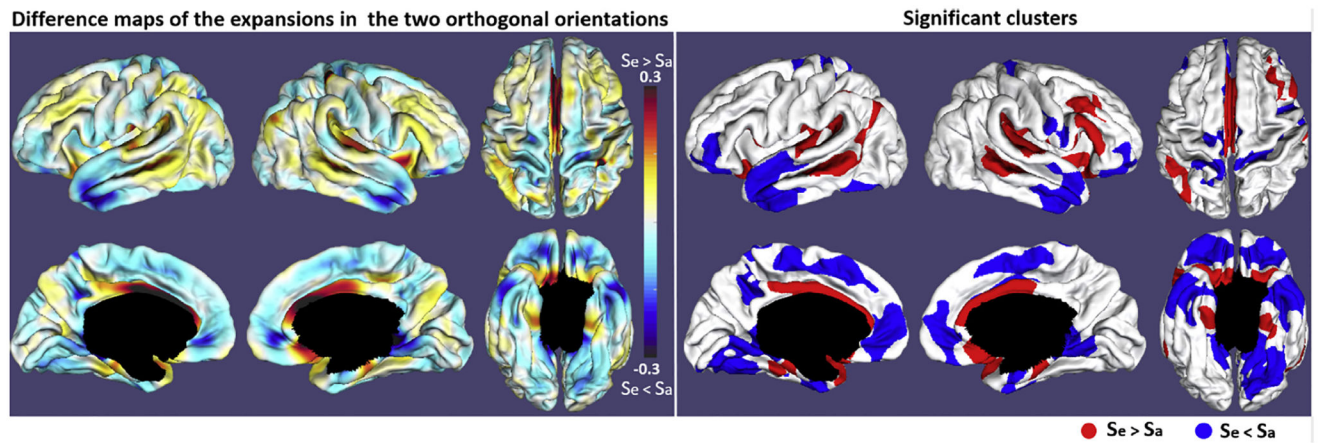


**Fig. 11.**

Differences between the cortical surface expansions perpendicular to folds and parallel to cortical folds. The left column shows difference maps. The right column shows the significant clusters ( $p < 0.05$ , after multiple comparisons correction). Red clusters indicate larger expansions in the orientation field perpendicular to cortical folds than in the orientation field parallel to cortical folds, and blue clusters indicate larger expansions in the orientation field parallel to cortical folds than in the orientation field perpendicular to cortical folds.

**Table 1**

The characteristics of the gradient field of sulcal depth and the maximum principal direction field.

<b>Region</b>	<b>Gyral crests and sulcal bottoms</b>		<b>Sulcal walls</b>	
	<b>Flat regions</b>	<b>Bended regions</b>	<b>Flat regions</b>	<b>Turning corners</b>
Gradient field of sulcal depth	Unreliable	Unreliable	<b>Reliable</b>	<b>Reliable</b>
Maximum principal direction field	Unreliable	<b>Reliable</b>	Unreliable	Unreliable
Gradient magnitude of sulcal depth	Small	Small	<b>Large</b>	<b>Large</b>
Absolute maximum principal curvature	Small	<b>Large</b>	Small	Large

The mean and standard deviation of the longitudinal cortical surface expansion perpendicular and parallel to cortical folds of the 30 subjects in the first postnatal year.

**Table 2**

Subjects	$s_e$		$s_n$	
	Left	Right	Left	Right
All (N = 30)	30.70 ± 9.55%	32.25 ± 10.06%	30.77 ± 9.37%	32.29 ± 10.18%
Male (N = 17)	29.53% ± 9.81%	30.73% ± 9.71%	30.43% ± 9.82%	30.92% ± 10.04%
Female (N = 13)	32.23% ± 10.25%	34.25% ± 12.16%	31.20% ± 9.71%	34.08% ± 11.73%